Vesiculation of healthy and defective red blood cells

He Li and George Lykotrafitis

Phys. Rev. E **92**, 012715 — Published 21 July 2015

DOI: 10.1103/PhysRevE.92.012715

Vesiculation of Healthy and Defective Red Blood Cells

He Li and George Lykotrafitis*
Department of Mechanical Engineering, University of Connecticut, Storrs, CT, USA.

Abstract

Vesiculation of mature red blood cells (RBCs) contributes to removal of defective patches of the erythrocyte membrane. In blood disorders, which are related to defects in proteins of the RBC membrane, vesiculation of the plasma membrane is intensified. Several hypotheses have been proposed to explain RBC vesiculation but the exact underlying mechanisms and what determines the sizes of the vesicles are still not completely understood. In this work, we apply a two-component coarse-grained molecular dynamics (CGMD) RBC membrane model to study how RBC vesiculation is controlled by the membrane spontaneous curvature and by lateral compression of the membrane. Our simulation results show that the formation of small homogeneous vesicles with a diameter less than 40 nm can be attributed to a large spontaneous curvature of membrane domains. On the other hand, compression on the membrane can cause the formation of vesicles with heterogeneous composition and with sizes comparable with the size of the cytoskeleton corral. When spontaneous curvature and lateral compression are simultaneously considered, the compression on the membrane tends to facilitate formation of vesicles originated from curved membrane domains. We also simulate vesiculation of RBCs with membrane defects connected to hereditary elliptocytosis (HE) and to hereditary spherocytosis (HS). When the vertical connectivity between the lipid bilayer and the membrane skeleton is elevated, as is in normal RBCs, multiple vesicles are shed from the compressed membrane with diameters similar to the cytoskeleton corral size. In HS RBC, where the connectivity between the lipid bilayer and the cytoskeleton is reduced, larger size vesicles are released under the same compression ratio as in normal RBCs. Lastly, we find that vesicles released from HE RBCs can contain cytoskeletal filaments due to fragmentation of the membrane skeleton while vesicles released from the HS RBCs are depleted of cytoskeletal filaments.

Corresponding Author: George Lykotrafitis, Department of Mechanical Engineering, The University of Connecticut, 191 Auditorium Road, Unit 3139, Storrs, CT 06269-3139, USA
Email: gelyko@engr.uconn.edu

Keywords: Nanovesicles, erythrocyte, coarse-grain molecular dynamics, spherocytosis, elliptocytosis

I. INTRODUCTION

RBCs circulate in the human body for nearly half million times during their approximately 120 days lifespan transporting oxygen from the lung to tissue cells and facilitating transport of carbon dioxide from tissue cells back to the lung. During their lifespan, erythrocytes lose approximately 20% of their surface area and lipid content mainly by shedding hemoglobin-containing vesicles [1,2]. Also, the vesiculation process is accelerated in patients with blood diseases such as HS and sickle cell disease (SCD) [3]. RBC-released vesicles are commonly grouped into two categories: nanovesicles and microvesicles, distinguished by their size. Nanovesicles have a mean diameter of approximately 25 nm [4-6] whereas microvesicles have diameters ranging from 60 to 300 nm [7]. It is believed that the production of nanovesicles is facilitated by the formation of membrane domains via the aggregation of specific types of membrane proteins or lipids which have mutual affinity [7]. If these membrane domains have significant spontaneous curvatures then they can bud off from the RBC membrane and form vesicles [7-9]. In line with this hypothesis, nanovesicles mainly contain lipids or proteins comprised in the membrane domains. Due to the small size of the nanovesicles (~25 nm), compared to the size of the cytoskeleton corrals (~90 nm), the formation of a nanovesicle should not be affected by the integrity of the RBC membrane skeleton [7]. On the other hand, formation of microvesicles is likely influenced by partial uncoupling between the lipid bilayer and the membrane skeleton [5,7,10]. Previous studies have shown that the RBC cytoskeleton is under stretch when tethered to the lipid bilayer and therefore exerts a compression force on the lipid bilayer [11,12]. This compression force is balanced by the bending resistance of the membrane [5,11]. As erythrocytes age, the stiffness of the cytoskeleton increase by 20% [13] and its density rise by 30-40% [14] leading to larger compressive forces on the cell membrane. It has then been hypothesized that the curvature of the membrane increases to accommodate the enlarged compression forces causing membrane buckling and formation of protuberances of sizes similar to the cytoskeleton corral-size. Subsequently, these protrusions grow further, as membrane particles flow towards them to relax the compression stress on the lipid bilayer, and finally detach from the membrane [15]. This could explain why the composition of the microvesicles is more heterogeneous than that of nanovesicles and similar to that of the parent RBC membrane [16-19].

Vesiculation of RBCs of patients suffering from the blood disorders of HS and HE is a complicated phenomenon due to defects appearing in various membrane proteins. The number of erythrocyte-released vesicles was found to increase in the blood content of patients with blood disorders [20-27]. In HS, defects in proteins that tether the cytoskeleton to the lipid bilayer, such as ankyrin, protein 4.2, and band-3 create areas in the RBC membrane which are not supported by the cytoskeleton [23,25]. In addition, the entropic elasticity of the spectrin filaments increases causing an increase in the cytoskeleton stiffness and consequently in the cytoskeleton-induced compression on the RBC membrane [28] facilitating vesiculation. As a result of the membrane loss, HS RBCs acquire a spherical shape. In HE, defects in cytoskeleton proteins such as α-spectrin, β-spectrin, and protein 4.1 cause disruption of the membrane skeleton and diminish its functionality as the main carrier of the loads applied to RBCs during blood circulation [24,29,30]. Also, HE RBCs cannot recover their original biconcave shape after they undergo large deformation in small capillaries and bloods vessels [20,22,25]. An additional effect of the skeleton partial disruption is that the RBC membrane may bud off and form vesicles at spectrin-deficient areas.

Several experimental studies have been conducted to investigate vesiculation of the RBC membrane. It has been shown that increase in the intracellular calcium concentration promoted shape transition of the RBC from discocyte to echinocyte [31,32] and that microvesicles were subsequently generated at the tips of echinocyte spicules [10,32,33]. A possible mechanism is that increase in intracellular calcium activates proteolytic enzymes, like calpain, which disrupt connections between the cytoskeleton and the lipid bilayer facilitating vesiculation [34]. Furthermore, depletion of adenosine triphosphate (ATP) in the RBC was found to induce cell morphological changes and vesiculation [18,32,35,36]. ATP-depletion potentially inhibits phosphorylation of the 4.1R protein, which facilitates the binding between spectrin and actin in its unphosphorylated state. This results in suppression of the dynamic remodeling of the cytoskeleton and therefore in increase of its stiffness [15,37]. It has also been found that the vesiculation process is accelerated in the blood disorders of HS and HE [3] meaning that defects in the membrane proteins facilitate vesiculation of the RBC membrane.

Analytical and numerical models have been developed to explain changes in the RBC shape and vesicle formation [5,11,15,38-43]. Sheetz and Singer [43] hypothesized that the sequential transition of stomatocyte–discocyte–echinocyte was induced by the area difference between the two leaflets of the plasma membrane. However, the area–difference–elasticity (ADE) model showed that as the area difference increased, the membrane tended to form protuberances instead of spicules [44]. This inconsistency was solved by introducing the elastic energy of the cytoskeleton into the ADE model [45-47]. Since the cytoskeleton is largely deformed during budding formation, the elastic energy of the cytoskeleton corresponding to budding is significantly increased and echinocytes have the preferred low-energy shape. Lim et al. [11] were able to model the entire stomatocyte–discocyte–echinocyte sequence by adding higher-order nonlinear terms in the ADE energy of the membrane skeleton. The authors also noted that the area difference term is equivalent to the spontaneous curvature term with regards to its effects on the cell shape because the spontaneous curvature can be naturally originated from the area difference between the two leaflets. Besides the area difference between the two leaflets of the lipid bilayer, the spontaneous curvature of the RBC membrane can be caused by many other factors including lipid molecules asymmetry [48], protein-lipid hydrophobic mismatch, and protein-assisted curvatures [49-51].

In addition to continuum mechanics-based models, several particle-based mesoscale models have also been developed to simulate the RBC membrane and lipid vesicles [52-57]. For example, Drouffe et al. [58] simulated lipid membranes in vesicles by introducing a one-particle-thick, solvent-free model in which the inter-particle interaction is described by a Lennard-Jones (LJ) type pair potential depending not only on the distance between the particles but also on their directionality. Noguchi and Gompper [59] developed a one-particle thick, solvent-free, lipid bilayer model by introducing a multibody potential that eliminated the need of the rotational degree of freedom introduced in [58]. Yuan et al. [60] introduced a similar approach, but instead of the LJ potential, a soft-core potential was used to better represent the particle self-diffusion. This membrane model was further applied to study the vesicle morphogenesis and domain organization [61]. A large number of studies have been conducted on particle-based models for the RBC membrane and lipid vesicles [62-68] but only few of them have focused on simulating RBC membrane vesiculation. Reynwar et al. [69] applied a coarse-grained membrane model to

show that curvature-induced by membrane proteins can drive protein clustering and subsequent formation of vesicles. Later, Spangler et al. [70] introduced a lipid membrane sphere model by combining a particle-based lipid bilayer model to an elastic meshwork to study cytoskeleton-induced blebbing. Their simulation results clearly demonstrated that membrane blebbing can be induced by disruption of the connections between the cytoskeleton and the lipid bilayer or by a uniform contraction of the cytoskeleton.

RBC membrane microvesiculation is likely due to the synergy of spontaneous curvature, compression, and membrane protein defects. For example, increased intracellular calcium or depleted ATP not only promotes asymmetry of leaflets but also activates proteolytic enzymes which break down the tethering of the lipid bilayer to the cytoskeleton increasing compression by the cytoskeleton [20]. In addition, it is known that the spontaneous curvatures and boundary line tension of lipid rafts or protein-enriched membrane domains can lead to a morphological transition of a membrane domain from flat to dimpled state [71,72]. However, how the spontaneous curvature of the membrane domain, the integrity of the spectrin network, the connectivity between the lipid bilayer and the membrane skeleton, and the interplay between them affect microvesiculation is not clear. In this work, we apply a previously developed two-component CGMD RBC membrane model [73] (see Fig. 1(a-c)) to investigate mechanisms of vesiculation of the normal RBC membrane and of the RBC membrane with protein defects. The applied model explicitly represents the lipid bilayer, band-3 proteins, and the cytoskeleton as CG particles. The model allows us to incorporate a variety of defects in the membrane and to introduce spontaneous curvature into the lipid bilayer. First, we simulate RBC membrane vesiculation induced by the spontaneous curvature of the membrane domain and vesiculation induced by the compression on the lipid bilayer respectively. Second, we simulate vesiculation of the RBC membrane due to the combined effects of the spontaneous curvature and of the compression on to the lipid bilayer. Lastly, we study vesiculation of RBCs with membrane protein defects that appear in HS and HE.

II. MODEL AND SIMULATION METHOD

The two-component CGMD human RBC membrane model applied in this work explicitly comprises both the lipid bilayer and the cytoskeleton. Three types of particles are introduced to represent the lipid bilayer (see Fig. 1(a)). The blue and yellow color particles represent clusters of lipid molecules and they have a diameter of 5 nm which is similar to the thickness of the lipid bilayer. The difference between the two types of lipid particles is related to the membrane spontaneous curvature and it will be discussed later. The black particles denote glycophorin proteins. They have the same diameter as the lipid particles. The third type particles signify band-3 complexes. One third of band-3 complexes, represented as light blue particles, are connected to the spectrin filaments. The rest of the band-3 complexes can diffuse in the lipid bilayer and they are represented as green particles. The cytoskeleton consists of spectrin filaments that are connected at actin junctions forming a canonical hexagonal network. An actin junction is represented by the red particle in Fig.1(a) and it is connected to the lipid bilayer via the glycophorin particle. Spectrin is a protein tetramer formed by a head-to-head association of two identical heterodimers which comprises an α-chain of 22 triple-helical segments and a β-chain of 17 triple-helical segments. In the proposed model, a spectrin filament is represented by

39 spectrin particles (white particles) connected by unbreakable springs [74]. A description of the configuration of the membrane and the employed potentials can be found in appendix 2 of this article and in the authors' previous work [73]. The lipid particles, the glycophorin particles, and the band-3 particles carry both translational and rotational degrees of freedom ($\mathbf{x}_i$, $\mathbf{n}_i$), where $\mathbf{x}_i$ and $\mathbf{n}_i$ are the position and the orientation (director vector) of particle i, respectively. The rotational degrees of freedom obey the normality condition $|\mathbf{n}_i| = 1$. $\mathbf{x}_{ij} = \mathbf{x}_j - \mathbf{x}_i$ is defined as the distance vector between particles i and j, with $r_{ij} \equiv |\mathbf{x}_{ij}|$ being the distance, and $\hat{\mathbf{x}}_{ij} = \mathbf{x}_{ij} / r_{ij}$ is a unit vector. The lipid particles, the glycophorin particles, and the band-3 particles interact with each other via a pair-wise additive potential

$$u_{mem}\left(\mathbf{n}_i, \mathbf{n}_j, \mathbf{x}_{ij}\right) = u_R\left(r_{ij}\right) + A\left(\alpha, a\left(\mathbf{n}_i, \mathbf{n}_j, \mathbf{x}_{ij}\right)\right) u_A\left(r_{ij}\right), \tag{1}$$

$$\begin{cases} u_R\left(r_{ij}\right) = \varepsilon\left(\left(R_{cut,mem} - r_{ij}\right) / \left(R_{cut,mem} - r_{eq}\right)\right)^8 & \text{for} \quad r_{ij} < R_{cut,mem} \\ u_A\left(r_{ij}\right) = -2\varepsilon\left(\left(R_{cut,mem} - r_{ij}\right) / \left(R_{cut,mem} - r_{eq}\right)\right)^4 & \text{for} \quad r_{ij} < R_{cut,mem} \\ u_R\left(r_{ij}\right) = u_A\left(r_{ij}\right) = 0, & \text{for} \quad r_{ij} \geq R_{cut,mem} \end{cases} \tag{2}$$

where $u_R(r_{ij})$ and $u_A(r_{ij})$ are the repulsive and attractive components of the pair potential, respectively. α is a tunable linear amplification factor and it is chosen to be 1.55 [73]. The function $A(\alpha, a(\mathbf{n}_i, \mathbf{n}_j, \mathbf{x}_{ij})) = 1 + \alpha(a(\mathbf{n}_i, \mathbf{n}_j, \mathbf{x}_{ij}) - 1)$ which tunes the energy well of the potential, regulates the fluid-like behavior of the membrane. The interaction between two CG particles depends not only on their distance but also on their relative orientation via the function $a\left(\mathbf{n}_i, \mathbf{n}_j, \mathbf{x}_{ij}\right)$ which varies from -1 to +1 and adjusts the attractive part of the potential. We specify that $a = 1$ corresponds to the case when $\mathbf{n}_i$ is parallel to $\mathbf{n}_j$ and both are normal to vector $\mathbf{x}_{ij}$ $\left(\left(\mathbf{n}_i \uparrow\uparrow \mathbf{n}_j\right) \perp \hat{\mathbf{x}}_{ij}\right)$, and the value $a = -1$ to the case when $\mathbf{n}_i$ is anti-parallel to $\mathbf{n}_j$ and both are perpendicular to vector $\mathbf{x}_{ij}$ $\left(\left(\mathbf{n}_i \uparrow\downarrow \mathbf{n}_j\right) \perp \hat{\mathbf{x}}_{ij}\right)$. The former instance is energetically favored due to the maximum attractive interaction between particles i and j, while the latter is energetically disfavored due to the maximum repulsive interaction. One simple form of $a\left(\mathbf{n}_i, \mathbf{n}_j, \mathbf{x}_{ij}\right)$ that captures these characteristics is

$$a\left(\mathbf{n}_i, \mathbf{n}_j, \hat{\mathbf{x}}_{ij}\right) = \left(\mathbf{n}_i \times \hat{\mathbf{x}}_{ij}\right) \cdot \left(\mathbf{n}_j \times \hat{\mathbf{x}}_{ij}\right) = \mathbf{n}_i \cdot \mathbf{n}_j - \left(\mathbf{n}_i \cdot \hat{\mathbf{x}}_{ij}\right)\left(\mathbf{n}_j \cdot \hat{\mathbf{x}}_{ij}\right) \tag{3}$$

The details of the applied potentials between the lipid CG particles were also discussed in [73,75]. A representation of the potential is plotted as the blue curve in Fig. 10 in appendix 2.

To introduce spontaneous curvature into our model, we modified the function $a\left(\mathbf{n}_i, \mathbf{n}_j, \mathbf{x}_{ij}\right)$ to

$$a(\mathbf{n}_i, \mathbf{n}_j, \hat{\mathbf{x}}_{ij}, \beta) = \mathbf{n}_i \cdot \mathbf{n}_j + (\beta - \mathbf{n}_i \cdot \hat{\mathbf{x}}_{ij})(\beta + \mathbf{n}_j \cdot \hat{\mathbf{x}}_{ij}) - 2\beta^2, \quad (4)$$

where β is the parameter that tunes the curvature of the lipid bilayer. The derivation of the Eq.(4) and the relation between β and the spontaneous curvature C are discussed in appendix 1. It was found that for small β the spontaneous curvature is given by $C_0 = 2^{5/6}\beta/\sigma$, where $\sigma = 5 \cdot 2^{-1/6}$ nm is the length unit of the system. In addition, in our model the motion of the lipid particles and of the integral membrane proteins is constrained when they move towards the negative z-direction by applying a harmonic potential. The potential is described as

$$V_{\text{confine}} = \frac{1}{2} K_{\text{confine}} z^2 \quad (5)$$

where K_{confine} is the confinement coefficient and z is the distance measured from the mid-plain of the supercell. K_{confine} is chosen to be ε/σ^2 . This additional constraint ensures the formation of exocytic and not enocytic vesicles, which have not been observed in adult human RBCs [76]. The potential acts only at the initiation of budding to impede penetration of the membrane skeleton by lipid and protein particles and thus to secure formation of protuberances away from the membrane skeleton.

The system consists of N = 32796 CG particles. The dimension of the membrane is approximately 0.8 μm × 0.8 μm. The temperature of the system is maintained at $k_B T/\varepsilon = 0.22$ by employing the Nose-Hoover thermostat. The model was implemented in the NAT ensemble [56,77,78]. Given that the diameter of the lipid particles is $r_{\text{eq}}^{\text{l-l}} = 2^{1/6} \cdot \sigma = 5\,\text{nm}$, the length unit σ is defined to be σ = 4.45 nm. The timescale that guides the choice of the timestep in the MD simulations is $t_s = \left(m_i d^2/\varepsilon\right)^{1/2}$. The timestep of the simulation is selected to be $\Delta t = 0.01 t_s$. Since the CG particles used in the simulations do not correspond to real molecules, the employed timescale can only be determined via comparison with experimental measurements. In our simulation, the timescale is established by measuring the viscosity of the membrane model and comparing it with the experimentally measured value for the RBC membrane. We found that the timescale is approximately $t_s \sim 3\times10^{-6} s$. For an independent confirmation, we also obtained the timescale by measuring the thermal fluctuation frequencies of the spectrin filaments and of the lipid membrane. The result was consistent with the timescale obtained from the viscosity measurements [73].

III. RESULTS AND DISCUSSION

A. Membrane vesiculation of the healthy RBC

1. Vesiculation due to spontaneous curvature of a membrane domain

Lipid rafts, have drawn significant attention as increasing evidence has shown that they play a crucial role in regulating cellular processes including cell polarity, protein trafficking, and signal transduction [71,79-84]. Membrane domains comprise specific type of proteins and lipids which

are more ordered and tightly packed than the surrounding bilayer. For example, lipid rafts in plasma membranes are enriched in sterol- and sphingolipids with size ranging from 10 to 200 nm [85-87], depending on the spontaneous curvatures, boundary line tension of lipid rafts, and diffusion of transmembrane proteins [71,72] or confinement of transmembrane proteins by the membrane skeleton [68]. In order to create phase separation and membrane domains in the applied RBC membrane model, we randomly assign each CG lipid particle to be of type F (blue) or G (yellow), as shown in Fig.1(b) and (c). The ratio between the populations of F and G particles is 1:4 and it is conserved throughout the simulations. Type G particles are considered to be a minority and clusters of G particles are treated as domains. The line tension between the two types of lipid particles F and G is simulated by assuming that the association energies between F-F and G-G particles are the same, but the association energy between F-G particles is only 70% of the association energy between F-F and G-G particles. We start the simulations with the two types of lipid particles completely mixed as shown in Fig. 1(b). Driven by the difference in association energies, G particles gradually aggregate to create small islands which then merge to form domains (see Fig. 1(c)). The domain size ranges from 20 to 100 nm, which is within the range of 10 to 200 nm observed in [85-87]. Then, we introduce spontaneous curvature into the potential energy of the membrane particles G by tuning the parameter β in Eq.(4). Fig. 2(a) shows that when $\beta = 0.1$, some membrane domains only slightly bulged out but no vesicles are formed meaning that the energy resulting from the line tension and spontaneous curvature is not large enough to drive vesiculation. As the spontaneous curvature increases, the membrane domains become more curved. For $\beta = 0.18$ vesiculation is observed. The released vesicle is made only of G type particles while its radius is about 16 nm (see Fig. 2(b)). This result indicates that the spontaneous curvature of the membrane domains has to be large enough to drive vesiculation while the vesicles induced by the spontaneous curvature have the same compositions as the corresponding membrane domains. Larger values of the parameter β result in the release of more vesicles with smaller sizes from the membrane. For example, when $\beta = 0.24$ the size of the formed vesicles is about 11nm (see Fig. 2(c)). Since the size of the vesicle decreases as the spontaneous curvature increases, we conclude that the maximum size of vesicles induced solely by the spontaneous curvature is obtained at $\beta = 0.18$. The corresponding diameter of the obtained vesicle is about 32 nm, which is consistent with the size of the nanovesicles (~25 nm), and smaller than the size of the microvesicles (60-300 nm) [88]. Because the vesicle size is smaller than the typical size of the cytoskeleton corral (~90 nm), we conjecture that the membrane skeleton does not affect vesiculation induced by spontaneous curvature [88].

2. Vesiculation due to lateral compression on the lipid bilayer

When lateral compression is applied on the RBC membrane model, the cytoskeleton shrinks while the lipid bilayer bends as it is incompressible. We define the compression ratio as the ratio of the decrease in horizontally projected area due to compression, to the projected area of the membrane at equilibrium and it is given by the expression $(A_0 - A)/A_0$, where A is the current

horizontally projected membrane area after compression and A_0 is the original projected membrane area at equilibrium. The compression ratios use in the simulations are selected to be $R_{\text{compression}}$ = 0.02, 0.05, 0.1, 0.15, and 0.18. The compression rate, which specifies how fast the projected area is reduced in the x and y direction, is chosen to be $0.01\sigma/t_s$.

To better understand our numerical results, we will examine them in the light of the Helfrich's membrane model [48]. The free energy function of the non-sheared RBC membrane is controlled by the membrane local curvature induced by thermal fluctuations, the spontaneous curvature, the line tension of membrane domains, and the cytoskeleton entropic elastic energy [11]. The expression for the free energy is described by

$$F = \kappa_b/2\int\left(C_1+C_2-C_0\right)^2 dA_l + \int \gamma dA_l + K_\alpha/2\int \alpha^2 dA_c \qquad (6)$$

where $(C_1+C_2)/2$ is the mean curvature originated from the thermal fluctuation of the membrane, C_0 is the spontaneous curvature, γ is the line tension at the boundary of the membrane domains, K_α is linear elastic moduli of the cytoskeleton and α is the cytoskeleton local area invariants [89].

Fig. 3(a) shows that when $R_{\text{compression}}$ = 0.02, only a small protuberance is created on the membrane while the cytoskeleton conforms to the protuberance. Under this condition, the free energy of the membrane is controlled by the bending energy of the lipid bilayer and the elastic energy of the cytoskeleton induced by the local stretch at the protuberant areas. As the compression ratio increases, the protuberance grows while the cytoskeleton continues following its shape until the stretching force is strong enough to pull off the cytoskeleton from the protrusion. The protrusion detaches from the cytoskeleton when $R_{\text{compression}}$ = 0.05 and 0.1. The corresponding free energy of the membrane is then only controlled by the bending energy of the lipid bilayer. At $R_{\text{compression}}$ = 0.15 the necks of the protrusions shrink and the formed vesicles are pinched off from the membrane to reduce the bending energy, as shown in the Fig. 3(c). The diameters of the two released vesicles are ~90 nm, which is similar to the size of the cytoskeleton corral and consistent with experimental observations in [20,23,90]. A larger compression ratio ($R_{\text{compression}}$ = 0.18) is also applied and it is found that three vesicles of similar sizes are created. Next, we examine the effects of the compression rates on the membrane vesiculation by employing the compression rates of $0.01\sigma/t_s$ and $0.001\sigma/t_s$. There are no noticeable differences between the compression processes at the small compression ratios of $R_{\text{compression}}$ = 0.02 and 0.05. When $R_{\text{compression}}$ is increased to 0.1 and the compression rate is high ($0.01\sigma/t_s$), several small protuberances are created and then diffuse to eventually merge to one big protrusion. In contrast, in the case of low compression rate ($0.001\sigma/t_s$), only one protuberance is formed initially and it gradually grows as the membrane is being compressed. At large compression ratios, such as $R_{\text{compression}}$ = 0.15 and 0.18, we find that when the compression rate is high ($0.01\sigma/t_s$) and $R_{\text{compression}}$ = 0.15, then multiple small protuberances are created at the beginning of the compression (see Fig. 4(a)). These protrusions either grow to form a vesicle (see Fig.4(b)) or merge to larger protuberances as the compression continues. Finally, two vesicles and one protuberance are observed (see Fig.4(c)). On the other hand, when the compression rate is low ($0.001\sigma/t_s$), only one protuberance is created at the beginning of the compression (see Fig.5(a)). As the compression continues to increase, this protrusion grows and eventually detaches from the membrane. After that, a second protrusion is formed (see Fig.5(b)). The vesiculation process is

repeated for this new protrusion and eventually two vesicles are finally obtained from membrane compression (see Fig.5(c)). In summary, for $R_{compression}$ = 0.15 and at low compression rate, the compression on the membrane causes formation of only two vesicles. However, when the compression rate is high then two smaller vesicles and one protrusion are created. Based on the above observations, we propose that the membrane compression rates could affect the size of the membrane-shed vesicles. When the compression rate is high, the compressed membrane tends to release small-sized vesicles as the fast compression does not allow the diffusion and merge of the protuberances. A membrane under slow compression could redistribute the induced bending energy and reach a lower energy state by coalescence of multiple small-size protuberances to large-size protuberances thus forming large size vesicles [5,7]. However, the vesicles obtained at the low compression rate are still much smaller than the microvesicles (up to diameter of 300 nm) observed in experiments. We hypothesize that, in normal RBCs, the larger-size microvesicles result from a compressed membrane with defects in the connections between band-3 and spectrin filaments. The defects could be due to depletion of ATP during the cell-aging process or during RBC storage. This mechanism of membrane vesiculation will be studied in the section 3.2.1 below.

3. Vesiculation due to the combined effects of spontaneous curvature and lateral compression

Above, we described results from our simulations on membrane vesiculation induced by the spontaneous curvature of membrane domains and by the lateral compression applied on the lipid bilayer. In this section, we discuss vesiculation of the RBC membrane under the combined effects of spontaneous curvature and compression. First, we simulate cases where the spontaneous curvature of the membrane domain is small and the domains only form protrusions but not vesicles. We find that when the spontaneous curvature is very small (β = 0.05), the vesiculation processes at $R_{compression}$ = 0.05 only produce a big protrusion as shown in Fig. 6(a), similar with the cases where no spontaneous curvature is introduced (see Fig. 3(b)). When $R_{compression}$ is increased to 0.15, vesicles consisting of two types of lipid particles are released. This means that small spontaneous curvatures do not affect the membrane vesiculation induced by the compression. However, when the spontaneous curvature is increased to β = 0.1, vesicles made of only G type lipid particles are observed at $R_{compression}$ = 0.05 and 0.1 (see Fig. 6(b) and 6(c)). When $R_{compression}$ = 0.05 and β = 0.1, one vesicles with size of ~60 nm is observed (see Fig. 6(b)). When $R_{compression}$ = 0.1, three vesicles are released from the membrane with sizes ranging from 40-60 nm, depending on the size of the originated membrane domains (see Fig. 6(c)). As shown in Fig. 2(a), when β = 0.1, the spontaneous curvature alone cannot drive vesiculation. Therefore we conclude that lateral compression promotes vesiculation of the curved membrane domain. In addition, it is noted that lateral compression on the membrane promotes buckling of the curved membrane domain instead of creating protrusions comprising two types of lipid particles like in the case of β = 0.05 under the same compression (see Fig. 6(a)). This finding is consistent with experimental observations that vesicles are preferentially shed from high curved regions, such as the tip of echinocyte spicules [10,32,33]. The large curvature of the membrane domain lower the energy cost to form a vesicle and thus increase the possibility of vesiculation [7]. As β increases, more vesicles made of only G lipid particles are released from the membrane at $R_{compression}$ = 0.05 and 0.1. For the cases of β >= 0.18, where the small-sized vesicles can be formed spontaneously without compression, our simulations show that when the membrane is

compressed at $R_{compression}$ = 0.05 and 0.1 then the curvature-driven small-sized vesicles are released from the membrane first and after that larger size vesicles stimulated by the compression are observed.

B. Vesiculation in the defective RBC membrane

In this section, we investigate how protein defects, as the ones appear in the HS and HE RBC, affect the vesiculation of the RBC membrane. Defects in the cytoskeleton proteins or in the proteins that tether the cytoskeleton to the lipid bilayer create areas in the membrane which are not supported by the cytoskeleton. RBCs with protein defects can lose these unsupported membrane areas by shedding vesicles [23]. It has been found that the population of erythrocyte-released vesicles is increased in the blood of patients with blood disorders [21-27,91]. Losing RBC membrane can alter cellular morphology, reduced cell deformability and early removal by the spleen [22,23].

1. Vesiculation due to compression on the HS RBC membrane

We simulate vesiculation of the RBC membrane with defects in the membrane proteins that tether the lipid bilayer to the spectrin network via vertical interactions. In particular, we explore the effect of the compression ratio and of the vertical connectivity on the number and size of formed vesicles. The defects are related to proteins such as band-3, protein 4.2, and ankyrin. They are usually found in HS RBCs [20,22,25]. However, defects in vertical interactions can be found in normal RBCs too as they can be induced by ATP depletion during RBC aging or during storage [7,36,92]. In our simulations, protein defects in the vertical interaction are represented by broken connections between immobile band-3 particles and spectrin filaments. We modify the vertical connectivity $C_{vertical}$ from 100% to 0% while the compression ratio $R_{compression}$ is selected to be 0.05, 0.1, 0.15, and 0.18. When the compression ratio is low ($R_{compression}$ = 0.05) only one protrusion is formed and no vesicle is released from the membrane for all selected $C_{vertical}$, similar to the result obtained from the normal RBC membrane (Fig. 7(a)). At higher compression ratio ($R_{compression}$ = 0.1), the unsupported budding area grows larger to accommodate the increased compression but vesiculation still does not occur (Fig. 7(c)). This is true for all selected $C_{vertical}$. When $R_{compression}$ is 0.15 or 0.18, we find that vesicles are formed for all values of $C_{vertical}$ as shown in the Fig. 7(c). However, the vesiculation process depends on the degree of membrane connectivity. At high $C_{vertical}$, the vesiculation starts from the area within the corral of the cytoskeleton and a vesicle is created with a size similar to the corral size (~90 nm). At low $C_{vertical}$, protrusions can migrate and merge to form larger protuberances and vesicles with an approximate size of 350 nm which is consistent with the higher end of the size range of microvesicles (60-300 nm) [7]. Our simulation results indicate that a large vertical connectivity $C_{vertical}$ of the RBC membrane slows down or prevents migration of the protrusions and thus favors the formation of vesicles with sizes similar to the size of the membrane skeleton corrals. In contrast, for low $C_{vertical}$ the size of the released vesicles is more diverse ranging from 90 nm to 350 nm since the constrain imposed by the cytoskeleton is lower. These observations can explain the large range of vesicle sizes shed by RBCs [7,20,23]. In addition, our simulations show that fragmentation of the cytoskeleton is not a necessary condition for vesiculation since

the formed vesicles are completely depleted of cytoskeleton components (see Fig.7(b)). This result is in agreement with experimental observations which show that vesiculation of healthy RBCs does not require fragmentation of the membrane skeleton but it can be enhanced by the uncoupling of the bilayer from the spectrin network [93]. Finally, we mention that while here we treat the compression ratio $R_{compression}$ independently of the vertical connectivity $C_{vertical}$, they can actually be coupled. Lower vertical connectivity stiffens the membrane skeleton resulting in an increased lateral pressure applied to the lipid bilayer by the membrane skeleton [28].

2. Vesiculation due to the compression on the HE RBC membrane

Lastly, we simulate vesiculation of the RBC membrane with defects in proteins, such as α-spectrin, β-spectrin, and protein 4.1, which are related to the integrity and elasticity of the cytoskeleton and appear in the membrane of HE RBCs. In particular, we explore the effect of the compression ratio and of the horizontal connectivity on the number and size of formed vesicles. In our model, the protein defects are represented as dissociations of spectrin chains at the spectrin dimer-dimer interactions and affect the horizontal interactions of the skeletal filaments. We implement the horizontal connectivities ($C_{horizontal}$) 0%, 20%, 40%, 60%, 80%, and 100% and the compression ratios $R_{compression}$ of 0.05, 0.1, and 0.15. The simulations show that for the low compression ratio of $R_{compression}$ = 0.05, only one protrusion is formed and no vesicles are released for all the selected $C_{horizontal}$ (Fig. 8(c)), similarly to cases of the normal RBC membrane and the HS RBC membrane. It is also noted that when the $C_{horizontal}$ is low, e.g. $C_{horizontal}$ = 20%, fragments of the cytoskeleton are observed to move within the protrusion as the cytoskeleton is largely disrupted (see Fig. 8(a)). When the higher compression ratio of $R_{compression}$ = 0.1 is applied, the unsupported protruding area grows but no vesiculation occurs for $C_{horizontal} \geq$ 60%. As the $C_{horizontal}$ decreases to 40%, vesicles are observed (Fig. 8(b)). We note that in the case of vertical connectivity reduction, however, there are no released vesicles from the HS RBC membrane for all selected $C_{vertical}$ at $R_{compression}$ = 0.1 (Fig. 7(c)). This difference in the vesiculation between the HS and HE RBC, at the same $R_{compression}$, indicates that the cytoskeleton plays a major role in maintaining the stability and integrity of the RBC membrane. Fig. 8(c) shows that when $R_{compression}$ is further increased to 0.15, vesiculation occurs for all the selected $C_{horizontal}$. Similarly to the results obtained in the HS RBC membrane. Two corral-size vesicles are created at high $C_{horizontal}$ ($C_{horizontal} \geq$ 60%) while one larger vesicle is found at low $C_{horizontal}$ ($C_{horizontal} \leq$ 40%). This difference is due to the reduction of the confinement of the lipid bilayer by the cytoskeleton as the cytoskeletal connectivity is reduced. We also found that vesicles released from the HE RBC membrane may contain cytoskeleton fragments (Fig. 8(b)) unlike vesicles shed from normal and HS RBCs which are depleted from the cytoskeleton components (Fig. 7(b)).

IV. Summary

We apply a two-component CGMD RBC membrane model to study vesiculation of the normal RBC membrane and of the HS and HE RBC membrane. We simulate vesiculation induced by the spontaneous curvatures of membrane domains and by the application of a lateral compression on the lipid bilayer. Our results and mechanisms are in agreement with predictions based on analytical modeling. In particular, we confirmed predictions related to vesicle sizes and the role of cytoskeleton connectivity and the composition of the lipid bilayer in RBC vesiculation

discussed in [5,7]. We show that the spontaneous curvatures of the RBC membrane domains can cause the formation of nanovesicles that comprise the same type of particles. Lateral compression on the membrane generates vesicles with size similar to the size of the cytoskeleton corral. When both effects are considered, the compression on the membrane tends to facilitate formation of vesicles that are made of the same type of lipid particles. Furthermore, we model vesiculation of the HS and HE RBC membrane by reducing the vertical and horizontal connectivities in our membrane model. We also show that the cytoskeleton plays a major role in the stability and integrity of the RBC membrane. We find that the size of the vesicles released from the HS and HE RBC membrane is more diverse than the size of the vesicles released from the normal RBC membrane. The reason for this difference is that the constrains induced by the cytoskeleton on the lipid bilayer of the defective RBC membrane are more moderate than the constrains induced in the normal RBC membrane. When the vertical or horizontal connectivity is large, multiple vesicles with size similar to the cytoskeleton corral size are formed at large compression ratios. In contrast, a membrane with low vertical or horizontal connectivity tends to shed vesicles of different sizes when it is largely compressed. We find that under the same compression ratio, membranes with protein defects in the horizontal interactions are more likely to shed vesicles than membranes with defects in the vertical interactions. We also note that vesicles released from the HE RBC membrane may contain fragments of the cytoskeleton while the vesicles shed from the HS RBC membrane are devoid of cytoskeleton components as the cytoskeleton filaments remain largely intact.

Acknowledgements
This work was supported by the National Science Foundation (CMMI-1235025, PHY-1205910) and the American Heart Association (12SDG12050688).

Appendix 1. Spontaneous curvature in the membrane model

To incorporate the spontaneous curvature into our model, we introduce a parameter β into the function $a(\mathbf{n}_i, \mathbf{n}_j, \mathbf{x}_{ij})$ defined in eq. (3). Then, the function $a(\mathbf{n}_i, \mathbf{n}_j, \mathbf{x}_{ij})$ becomes

$$a(\mathbf{n}_i, \mathbf{n}_j, \hat{\mathbf{x}}_{ij}, \beta) = \mathbf{n}_i \cdot \mathbf{n}_j - (\mathbf{n}_i \cdot \hat{\mathbf{x}}_{ij})(\mathbf{n}_j \cdot \hat{\mathbf{x}}_{ij}) + \beta(\mathbf{n}_i - \mathbf{n}_j) \cdot \hat{\mathbf{x}}_{ij} + c(\beta).$$

$a(\mathbf{n}_i, \mathbf{n}_j, \hat{\mathbf{x}}_{ij}, \beta)$ takes its maximum value +1 when $\mathbf{n}_i$ forms an angle of $\pi/2 + \theta_0/2$ with $\hat{\mathbf{x}}_{ij}$ and symmetrically to $\mathbf{n}_j$, as shown in Fig.9. Since the above expression is vectorial and frame-independent, we pick $\hat{\mathbf{x}}_{ij} = \mathbf{e}_x$ in order to simplify the following discussion. Then, α takes the form

$$a = n_i^y n_j^y + n_i^z n_j^z + \beta(n_j^x - n_i^x) + c(\beta).$$

Next, we maximize a under the normalization constraints

$$(n_i^x)^2 + (n_i^y)^2 + (n_i^z)^2 = (n_j^x)^2 + (n_j^y)^2 + (n_j^z)^2 = 1.$$

Since y and z appear always together, we set $n_i^y = n_j^y = 0$ to further simplify the maximization process. Then α takes the form

$$a = n_i^z n_j^z + \beta(n_j^x - n_i^x) + c(\beta),$$

with

$(n_i^x)^2 + (n_i^z)^2 = (n_j^x)^2 + (n_j^z)^2 = 1$, which gives $n_i^z = n_j^z = \sqrt{1 - (n_j^x)^2}$, since $n_i^x = -n_j^x$.

Thus,

$$a = 1 - (n_j^x)^2 + 2\beta n_j^x + c(\beta),$$

and the optimal choice for maximum $a = +1$ is $n_j^{x,opt} = \beta$, with $c(\beta) = -\beta^2$, while β can be identified geometrically as $\beta = \sin(\theta_0/2)$.

Finally, a takes the form

$$a(\mathbf{n}_i, \mathbf{n}_j, \hat{\mathbf{x}}_{ij}, \beta) = \mathbf{n}_i \cdot \mathbf{n}_j - (\mathbf{n}_i \cdot \hat{\mathbf{x}}_{ij})(\mathbf{n}_j \cdot \hat{\mathbf{x}}_{ij}) + \beta(\mathbf{n}_i - \mathbf{n}_j) \cdot \hat{\mathbf{x}}_{ij} - \beta^2,$$

which can be rewritten as

$$a(\mathbf{n}_i,\mathbf{n}_j,\hat{\mathbf{x}}_{ij},\beta)=\mathbf{n}_i\cdot\mathbf{n}_j+(\beta-\mathbf{n}_i\cdot\hat{\mathbf{x}}_{ij})(\beta+\mathbf{n}_j\cdot\hat{\mathbf{x}}_{ij})-2\beta^2$$

When the equilibrium angle between the direction vectors of two interacting particles is θ_0, the corresponding spontaneous curvature of the membrane is $C_0 = \theta_0/(2^{1/6}\sigma)$, where σ is the length unit of the system. Since $\beta=\sin(\theta_0/2)$, then $\beta\sim\theta_0/2$ for small β. Consequently, we find that $C_0 = 2^{5/6}\beta/\sigma$.

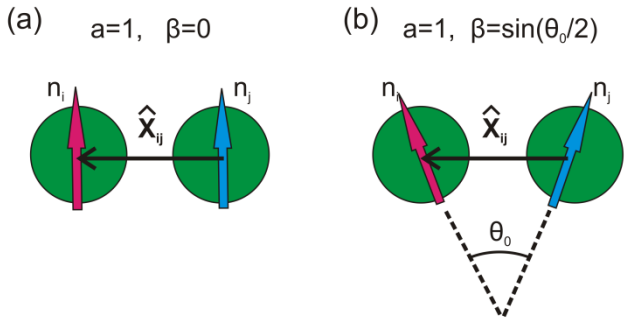

Figure 9. Geometry of two interacting CG particles *i* and *j* when $a(\mathbf{n}_i,\mathbf{n}_j,\hat{\mathbf{x}}_{ij},\beta)$ = 1 with (a) $\beta=0$ and (b) $\beta=\sin(\theta_0/2)$.

Appendix 2. Brief introduction of the applied RBC membrane model

The membrane of the RBC consists of spectrin tetramers which are connected at actin junctional complexes forming a 2D six-fold triangular network anchored to the lipid bilayer. Spectrin is a protein tetramer formed by a head-to-head association of two identical heterodimers. Each heterodimer consists of an α-chain with 22 triple-helical segments and a β-chain with 17 triple-helical segments. In the applied model, a spectrin filament is represented by 39 particles connected by unbreakable harmonic springs. Thus, the equilibrium distance between the spectrin particles is $r_{eq}^{s\text{-}s}=L_{max}/39$, where L_{max} is the contour length of the spectrin (~200 nm), and $r_{eq}^{s\text{-}s}\cong 5$ nm. The spectrin network model employed here is similar to the one illustrated in [74]. Three types of CG particles are introduced to represent lipids and band-3 proteins. The blue color particles denote a cluster of lipid molecules. Their diameter of 5 nm is approximately equal to the thickness of the lipid bilayer. The black particles represent glycophorin proteins with the same diameter as the lipid particles. Band-3 protein comprises two domains: (i) the cytoplasmic domain with a dimension of 7.5×5.5×4.5nm that contains the binding sites for the cytoskeletal

proteins, and (ii) the membrane domain, with a dimension of 6×11×8 nm, whose main function is to mediate anion transport. We represent the membrane domain of band-3 as a spherical CG particle with a radius of 5 nm. The volume of the particle is similar to the excluded volume of the membrane domain of a band-3. However, when band-3 proteins interact with the cytoskeleton, the effect of the cytoplasmic domain has to be taken into account. In this case the effective radius is considered approximately 12.5 nm.

As mentioned above, spectrin is represented by 39 spectrin particles connected by unbreakable springs. The spring potential $u_{cy}^{s\text{-}s}(r) = k_0(r - r_{eq}^{s\text{-}s})^2 / 2$ is depicted by the green curve in Fig. 10. The equilibrium distance between the spectrin particles is $r_{eq}^{s\text{-}s} \cong 5$ nm. The two ends of the spectrin chains are connected to the actin junctional complexes via the spring potential $u_{cy}^{a\text{-}s}(r) = k_0(r - r_{eq}^{a\text{-}s})^2 / 2$, where the equilibrium distance between an actin and a spectrin particle is $r_{eq}^{a\text{-}s} = 10$ nm. The potential is plotted as the red curve in Fig. 10. The spring constant $k_0 = 57\ \varepsilon/\sigma^2$ is chosen to be identical with the curvature of $u_{LJ}(r_{ij}) = 4\varepsilon\left[\left(\sigma / r_{ij}\right)^{12} - \left(\sigma / r_{ij}\right)^{6}\right] + \varepsilon$ at the bottom of the energy well to reduce the number of free parameters. Spectrin particles that are not connected by the spring potential interact with each other via the repulsive part of the L-J potential

$$u_{rep}(r_{ij}) = \begin{cases} 4\varepsilon\left[\left(\dfrac{\sigma}{r_{ij}}\right)^{12} - \left(\dfrac{\sigma}{r_{ij}}\right)^{6}\right] + \varepsilon & r_{ij} < R_{cut,LJ} = r_{eq}^{s\text{-}s} \\ 0 & r_{ij} > R_{cut,LJ} = r_{eq}^{s\text{-}s} \end{cases}$$

where ε is the energy unit and σ is the length unit. r_{ij} is the distance between spectrin particles. The cutoff distance of the potential $R_{cut,LJ}$ is chosen to be the equilibrium distance $r_{eq}^{s\text{-}s}$ between two spectrin particles. The potential is shown as the black curve in Fig.10.

The applied two-component membrane model consists of N = 29567 CG particles. The dimension of the membrane is approximately 0.8 μm × 0.8 μm. The numerical integrations of the equations of motion for all the particles in the simulation are performed using the Beeman algorithm. The temperature of the system is maintained at $k_B T/\varepsilon = 0.22$ by employing the Nose-Hoover thermostat. The model is implemented in the NAT ensemble. Periodic boundary conditions are applied in all three directions. Since the model is solvent-free and the membrane is a two-dimensional structure, we controlled the projected area instead of the volume. The projected area is adjusted to result in zero tension for the entire system at the equilibrium state.

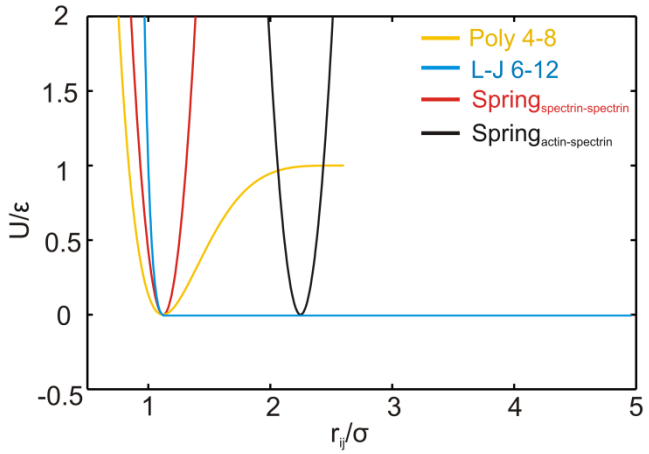

Figure. 10. Interaction potentials employed in the membrane model. The yellow curve represents the pair-wise potential between lipid particles. The red curve represents the spring potential between spectrin particles. The black curve represents the spring potential between actin and spectrin particles. The light blue curve represents the repulsive L-J potential between lipid and spectrin particles.

Figure Captions

Figure 1. (a) Schematic of the human RBC membrane. The blue and yellow spheres represent two types of lipid particles corresponding to membrane areas with different spontaneous curvatures. The red sphere signifies an actin junctional complex. The white sphere represents a spectrin particle and the black sphere represents a glycophorin particle. The light blue circle corresponds to a band-3 complex which is connected to the spectrin network while the green circle represents a band-3 complex which is not connected to the lipid bilayer. (b) Top view of the membrane model with the two types of CG lipid particles completely mixed. (c) Top view of the membrane model after the "G" type particles aggregate into membrane domains. “A” type particles represent actin junctional complexes, “B” type particles represent spectrin segments, “C” type particles represent glycophorin proteins, “D” type particles represent band-3 complexes that

are connected to the spectrin network ("immobile" band-3), "E" type particles represent free band-3 proteins that are not connected to the network ("mobile" band-3), "F" and "G" type particles represent lipid clusters.

Figure 2. Vesiculation induced by the spontaneous curvature of membrane domains. (a) When the spontaneous curvature is small (β = 0.1), the membrane domains only bulge out from the membrane but no vesicle is formed. (b) When β increases to 0.18, vesiculation occurs and the released vesicles are only made of G type particles. (c) When β is increased to 0.24, a larger number of vesicles are released from the membrane.

Figure 3. Vesiculation induced by a lateral compression applied on the lipid bilayer. (a) When the compression ratio is $R_{\text{compression}}$ = 0.02, only a small protrusion is created on the membrane and the cytoskeleton conforms to the protrusion. (b) When $R_{\text{compression}}$ is increased to 0.05, the protrusion grows and the cytoskeleton retracts from the protuberant area. (c) When $R_{\text{compression}}$ is increased to 0.15, two vesicles are released from the membrane.

Figure 4. Vesiculation induced by a lateral compression applied on the lipid bilayer at the compression ratio of $R_{\text{compression}}$ = 0.15 and at the compression rate of $0.01\sigma/t_s$. (a) Multiple protuberances are created at the beginning of the compression. (b) The obtained protuberances either grow to form a vesicle or merge to produce larger protuberances as the compression continues. (c) Finally, two vesicles and a protrusion are observed.

Figure 5. Vesiculation induced by a lateral compression applied on the lipid bilayer at the compression ratio of $R_{\text{compression}}$ = 0.15 and at the compression rate of $0.001\sigma/t_s$. (*a*) Only one protuberance is created at the beginning of the compression. (b) As the compression continues, the protrusion grows and a vesicle is formed. Then, a second protrusion is generated and the vesiculation process is repeated. (c) Finally, two vesicles are released from the membrane.

Figure 6. Vesiculation induced by the combined effects of the spontaneous curvature of the membrane and of the lateral compression applied on the membrane. (a) When the spontaneous curvature is very small (β = 0.05), then a big protuberance is formed at the compression ratio of $R_{\text{compression}}$ = 0.05. (b) When the spontaneous curvature is increased to β = 0.1 while the compression ratio remains at $R_{\text{compression}}$ = 0.05, then one vesicle is released. The vesicle has a size of ~60 nm and comprises only G type lipid particles. (c) When the compression ratio $R_{\text{compression}}$ increases to 0.1 and the spontaneous curvature parameter is β = 0.1, then three vesicles are released from the membrane with sizes ranging from 40-60 nm.

Figure 7. Vesiculation of the membrane with protein defects in the vertical interactions. (a) When the compression ratio $R_{\text{compression}}$ is low ($R_{\text{compression}}$ = 0.05), only one protuberance is formed for all the selected vertical connectivities C_{vertical}. (b) When $R_{\text{compression}}$ = 0.15 and the vertical connectivity is C_{vertical} = 60%, one vesicle and one big protuberance are obtained. (c) Diagram showing the dependence of the number of formed vesicles from the vertical connectivity and the compression ratio. × indicates that no vesiculation occurs. , , and indicate that one, two, and three vesicles are formed respectively.

Figure 8. Vesiculation of the membrane with protein defects in the horizontal interactions. (a) When the compression ratio is $R_{\text{compression}}$ = 0.05 and the horizontal connectivity is $C_{\text{horizontal}}$ = 20%, only one protuberance is formed in the membrane. (b) When $R_{\text{compression}}$ = 0.1 and $C_{\text{horizontal}}$ = 40%, one vesicle enclosing a cytoskeleton fragment is formed. (c) Diagram showing the dependence of the number of formed vesicles from the horizontal connectivity and the compression ratio. × indicates that no vesiculation occurs. □ indicates that one vesicle is formed. □ indicates that two vesicles are formed.

Figure 9. Geometry of two interacting CG particles *i* and *j* when $a\left(\mathbf{n}_i, \mathbf{n}_j, \hat{\mathbf{x}}_{ij}, \beta\right) = 1$ with (a) $\beta = 0$ and (b) $\beta = \sin\left(\theta_0/2\right)$.

Figure 10. Interaction potentials employed in the membrane model. The yellow curve represents the pair-wise potential between lipid particles. The red curve represents the spring potential between spectrin particles. The black curve represents the spring potential between actin and spectrin particles. The light blue curve represents the repulsive L-J potential between lipid and spectrin particles.

References

[1] F. L. Willekens, B. Roerdinkholder-Stoelwinder, Y. A. Groenen-Dopp, H. J. Bos, G. J. Bosman, A. G. van den Bos, A. J. Verkleij, and J. M. Werre, Blood **101**, 747 (2003).

[2] F. L. A. Willekens, J. M. Werre, Y. A. M. Groenen-Döpp, B. Roerdinkholder-Stoelwinder, B. De Pauw, and G. J. C. G. M. Bosman, British Journal of Haematology **141**, 549 (2008).

[3] N. S. Barteneva, E. Fasler-Kan, M. Bernimoulin, J. N. Stern, E. D. Ponomarev, L. Duckett, and I. A. Vorobjev, BMC Cell Biol. **14**, 23 (2013).

[4] A. Roux, D. Cuvelier, P. Nassoy, J. Prost, P. Bassereau, and B. Goud, EMBO J. **24**, 1537 (2005).

[5] P. Sens and N. Gov, Physical Review Letters **98**, 018102 (2007).

[6] F.-C. Tsai and H.-Y. Chen, Physical Review E **78**, 051906 (2008).

[7] N. Gov, J. Cluitmans, P. Sens, and G. J. C. G. M. Bosman, in *Advances in Planar Lipid Bilayers and Liposomes* (Elsevier Inc, Burlington, 2009), pp. 95.

[8] P. F. Devaux, Biochimie **82**, 497 (2000).

[9] P. Sens, Physical Review Letters **93**, 108103 (2004).

[10] S. C. Liu, D. L. H, D. M. A, and P. J Eur J Cell Biol **49**, 358 (1989).

[11] H. W. G. Lim, M. Wortis, and R. Mukhopadhyay, Proceedings of the National Academy of Sciences of the United States of America **99**, 16766 (2002).

[12] D. E. Discher, D. H. Boal, and S. K. Boey, Biophysical Journal **75**, 1584 (1998).

[13] K. Fricke and E. Sackmann, Biochim Biophys Acta **803**, 145 (1984).

[14] C. Edwards *et al.*, International Journal of Behavioral Medicine **12**, 171 (2005).

[15] N. S. Gov and S. A. Safran, Biophysical Journal **88**, 1859 (2005).

[16] D. Allan, M. M. Billah, J. B. Finean, and R. H. Michell, Nature **261**, 58 (1976).

[17] A. Elgsaeter, D. M. Shotton, and D. Branton, Biochimica et Biophysica Acta (BBA) - Biomembranes **426**, 101 (1976).

[18] H. U. Lutz, S. C. Liu, and J. Palek, J. Cell Biol. **73**, 548 (1977).

[19] H. Hägerstrand and B. Isomaa, Biochim Biophys Acta. **1190**, 409 (1994).

[20] A. Alaarg, R. Schiffelers, W. W. van Solinge, and R. Van Wijk, Frontiers in Physiology **4** (2013).

[21] W. T. Tse, M. C. Lecomte, F. F. Costa, M. Garbarz, C. Feo, P. Boivin, D. Dhermy, and B. G. Forget, Journal of Clinical Investigation **86**, 909 (1990).

[22] W. T. Tse and S. E. Lux, British Journal of Haematology **104**, 2 (1999).

[23] S. Eber and S. Lux, E., Semin. Hematol. **41**, 118 (2004).

[24] P. G. Gallagher, Semin. Hematol. **41**, 142 (2004).

[25] X. An and N. Mohandas, British Journal of Haematology **141**, 367 (2008).

[26] L. D. Walensky, N. Mohandas, and S. E. Lux, in *Blood - Principles and Practice in Hematology - Herediatery Spherocytosis*, edited by R. I. Handin, S. E. Lux, and T. P. Stossel (Lippincott Williams & Wilkins, 2003).

[27] N. Mohandas and P. G. Gallagher, Blood **112**, 3939 (2008).

[28] N. S. Gov, New Journal of Physics **9** (2007).

[29] S.-C. Liu, J. Palek, and T. J. Prchal, Proceedings of the National Academy of Sciences of the United States of America **79**, 2072 (1982).

[30] J. Palek, Clinics in haematology **1**, 45 (1985).

[31] E. M. Bevers, T. Wiedmer, P. Comfurius, S. J. Shattil, H. J. Weiss, R. F. Zwaal, and P. J. Sims, Blood **79**, 380 (1992).
[32] T. J. Greenwalt, Transfusion **46**, 143 (2006).
[33] W. H. Reinhart and S. Chien, American Journal of Hematology **24**, 1 (1987).
[34] O. Morel, J. Laurence, F. Jean-Marie, and T. Florence, Arteriosclerosis, Thrombosis, and Vascular Biology. **31**, 15 (2011).
[35] U. Salzer, R. Zhu, M. Luten, H. Isobe, V. Pastushenko, T. Perkmann, P. Hinterdorfer, and G. J. C. G. M. Bosman, Transfusion **48**, 451 (2008).
[36] J. R. Hess, Transfus Apher Sci **43**, 51 (2010).
[37] N. S. Gov, Physical Review E **75**, 011921 (2007).
[38] U. Seifert, K. Berndl, and R. Lipowsky, Physical Review A **44**, 1182 (1991).
[39] U. Seifert and R. Lipowsky, in *Structure and dynamics of membranes: From cells to vesicles*, edited by A. J. Hoff (Elsevier, Amsterdam, 1995).
[40] U. Seifert, Advances in Physics **46**, 13 (1997).
[41] J.-Y. Tinevez, U. Schulze, G. Salbreux, J. Roensch, J.-F. Joanny, and E. Paluch, Proceedings of the National Academy of Sciences **106**, 18581 (2009).
[42] J. Young and S. Mitran, Journal of Biomechanics **43**, 210 (2010).
[43] M. P. Sheetz and S. J. Singer, Proceedings of the National Academy of Sciences **71**, 4457 (1974).
[44] L. Miao, U. Seifert, M. Wortis, and H. G. Döbereiner, Physical Review E **49**, 5389 (1994).
[45] R. E. Waugh, Biophysical Journal **70**, 1027 (1996).
[46] A. Iglič, Journal of Biomechanics **30**, 35 (1997).
[47] R. Mukhopadhyay, H. W. Gerald Lim, and M. Wortis, Biophysical Journal **82**, 1756 (2002).
[48] W. Helfrich, Zeitschrift Fur Naturforschung C-a Journal of Biosciences **C28**, 693 (1973).
[49] B. J. Reynwar, G. Illya, V. A. Harmandaris, M. M. Muller, K. Kremer, and M. Deserno, Nature **447**, 461 (2007).
[50] P. D. Blood and G. A. Voth, Proceedings of the National Academy of Sciences **103**, 15068 (2006).
[51] J. Zimmerberg and M. M. Kozlov, Nat Rev Mol Cell Biol **7**, 9 (2006).
[52] R. Goetz, G. Gompper, and R. Lipowsky, Physical Review Letters **82**, 221 (1999).
[53] H. Noguchi and M. Takasu, Biophysical Journal **83**, 299 (2002).
[54] G. Brannigan, P. F. Philips, and F. L. H. Brown, Physical Review E **72**, 011915 (2005).
[55] I. R. Cooke, K. Kremer, and M. Deserno, Physical Review E **72**, 011506 (2005).
[56] Z. J. Wang and D. Frenkel, Journal of Chemical Physics **122**, 234711 (2005).
[57] O. Farago, Journal of Chemical Physics **119**, 596 (2003).
[58] J. M. Drouffe, A. C. Maggs, and S. Leibler, Science **254**, 1353 (1991).
[59] H. Noguchi and G. Gompper, Physical Review E **73**, 021903 (2006).
[60] H. Yuan, C. Huang, J. Li, G. Lykotrafitis, and S. Zhang, Physical Review E **82**, 011905 (2010).
[61] C. Huang, H. Yuan, and S. Zhang, Applied Physics Letters **98**, 043702 (2011).
[62] G. Brannigan, L. C. L. Lin, and F. L. H. Brown, European Biophysics Journal with Biophysics Letters **35**, 104 (2006).
[63] M. Muller, K. Katsov, and M. Schick, Physics Reports **434**, 113 (2006).

[64] M. Venturoli, M. M. Sperotto, M. Kranenburg, and B. Smit, Physics Reports-Review Section of Physics Letters **437**, 1 (2006).
[65] W. F. D. Bennett and D. P. Tieleman, Biochimica et Biophysica Acta (BBA) - Biomembranes **1828**, 1765 (2013).
[66] Z. Peng, X. Li, I. V. Pivkin, M. Dao, G. E. Karniadakis, and S. Suresh, Proc Natl Acad Sci U S A **110**, 13356 (2013).
[67] I. V. Pivkin and G. E. Karniadakis, Phys Rev Lett **101**, 118105 (2008).
[68] M. K. Sikder, K. A. Stone, P. B. Kumar, and M. Laradji, J Chem Phys **141**, 054902 (2014).
[69] B. J. Reynwar, G. Illya, V. A. Harmandaris, M. M. Muller, K. Kremer, and M. Deserno, Nature **447**, 461 (2007).
[70] E. J. Spangler, C. W. Harvey, J. D. Revalee, P. B. S. Kumar, and M. Laradji, Physical Review E **84**, 051906 (2011).
[71] T. S. Ursell, W. S. Klug, and R. Phillips, Proceedings of the National Academy of Sciences **106**, 13301 (2009).
[72] H. Yuan, C. Huang, and S. Zhang, BioNanoSci. **1**, 97 (2011).
[73] H. Li and G. Lykotrafitis, Biophysical Journal **107**, 642 (2014).
[74] J. Li, G. Lykotrafitis, M. Dao, and S. Suresh, Proc Natl Acad Sci U S A **104**, 4937 (2007).
[75] H. Li and G. Lykotrafitis, Biophysical Journal **102**, 75 (2012).
[76] R. Schekman and S. J. Singer, Proc Natl Acad Sci U S A **73**, 4075 (1976).
[77] A. Imparato, J. C. Shillcock, and R. Lipowsky, Europhysics Letters **69**, 650 (2005).
[78] R. Goetz and R. Lipowsky, Journal of Chemical Physics **108**, 7397 (1998).
[79] P. B. Sunil Kumar, G. Gompper, and R. Lipowsky, Physical Review Letters **86**, 3911 (2001).
[80] M. Laradji and P. B. Sunil Kumar, Physical Review Letters **93**, 198105 (2004).
[81] M. Laradji and P. B. Sunil Kumar, The Journal of Chemical Physics **123** (2005).
[82] M. Laradji and P. B. Kumar, Physical Review E **73**, 040901 (2006).
[83] M. Yanagisawa, M. Imai, T. Masui, S. Komura, and T. Ohta, Biophysical Journal **92**, 115 (2007).
[84] S. Ramachandran, M. Laradji, and P. B. S. Kumar, Journal of the Physical Society of Japan **78**, 041006 (2009).
[85] M. Edidin, Annual Review of Biophysics and Biomolecular Structure **32**, 257 (2003).
[86] K. Simons and W.L.C. Vaz, Annual Review of Biophysics and Biomolecular Structure **33**, 269 (2004).
[87] K. Jacobson, O. G. Mouritsen, and R. G. W. Anderson, Nat Cell Biol **9**, 7 (2007).
[88] T. Auth and N. S. Gov, Biophysical Journal **96**, 818 (2009).
[89] E. A. Evans and R. Skalak, *Mechanics and thermodynamics of biomembranes* (CRC Press, 1980, 1980).
[90] S. E. Lux, British Journal of Haematology, **104**, 2 (1999).
[91] M. Westerman *et al.*, British Journal of Haematology **142**, 126 (2008).
[92] R. Obrador, S. Musulin, and B. Hansen, J Vet Emerg Crit Care (San Antonio) (2014).
[93] D. W. Knowles, L. Tilley, N. Mohandas, and J. A. Chasis, Proceedings of the National Academy of Sciences **94**, 12969 (1997).

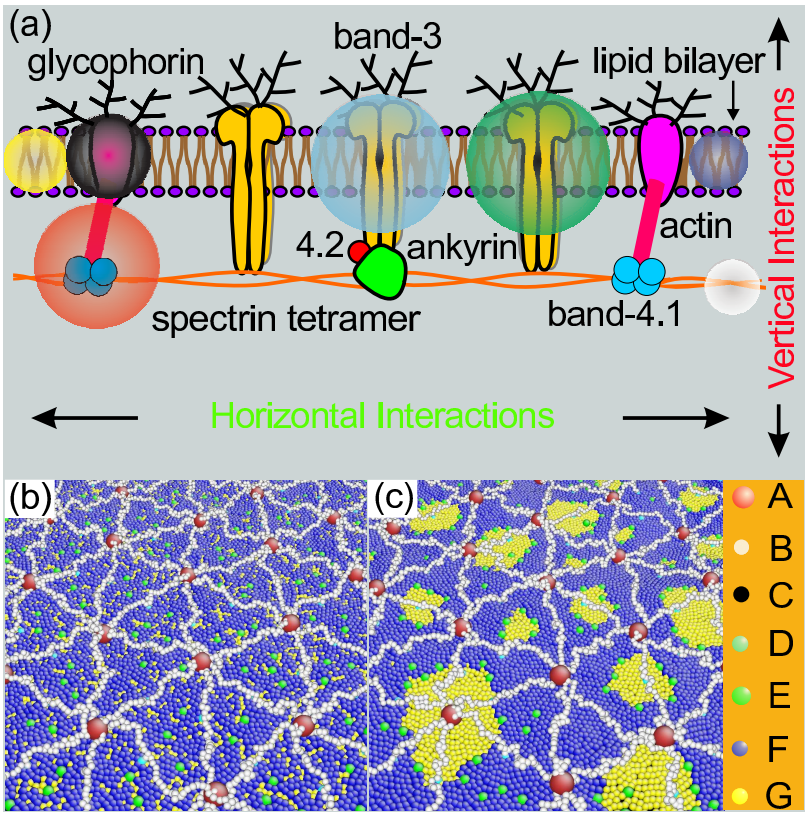

Figure 1 EC11454 23JUN2015

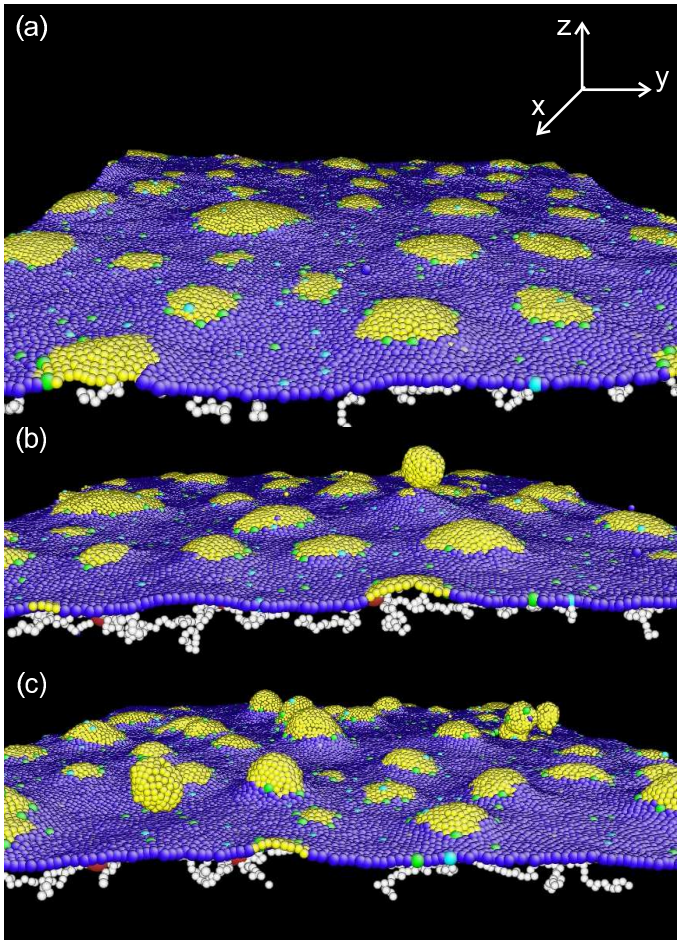

Figure 2 EC11454 23JUN2015

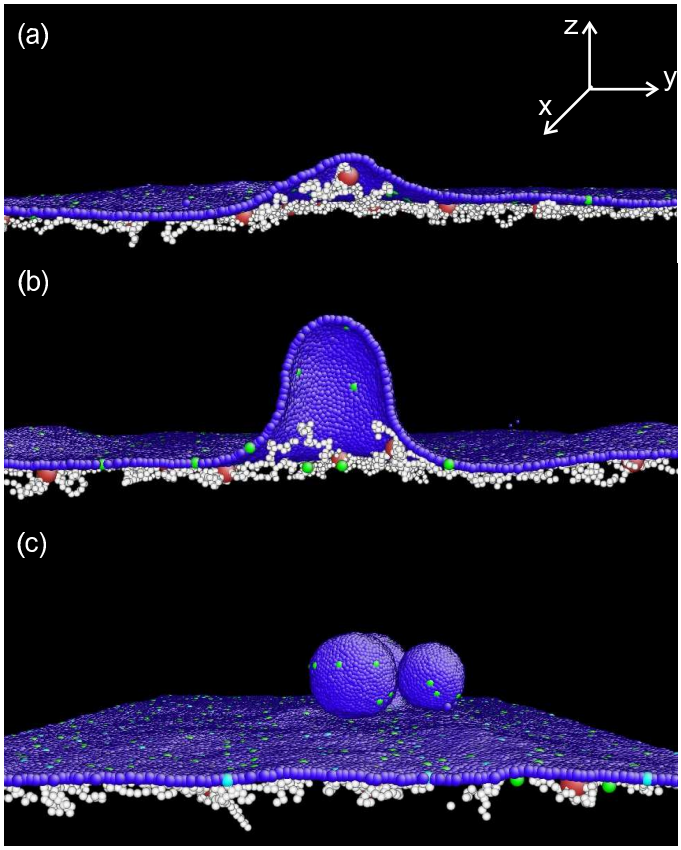

Figure 3 EC11454 23JUN2015

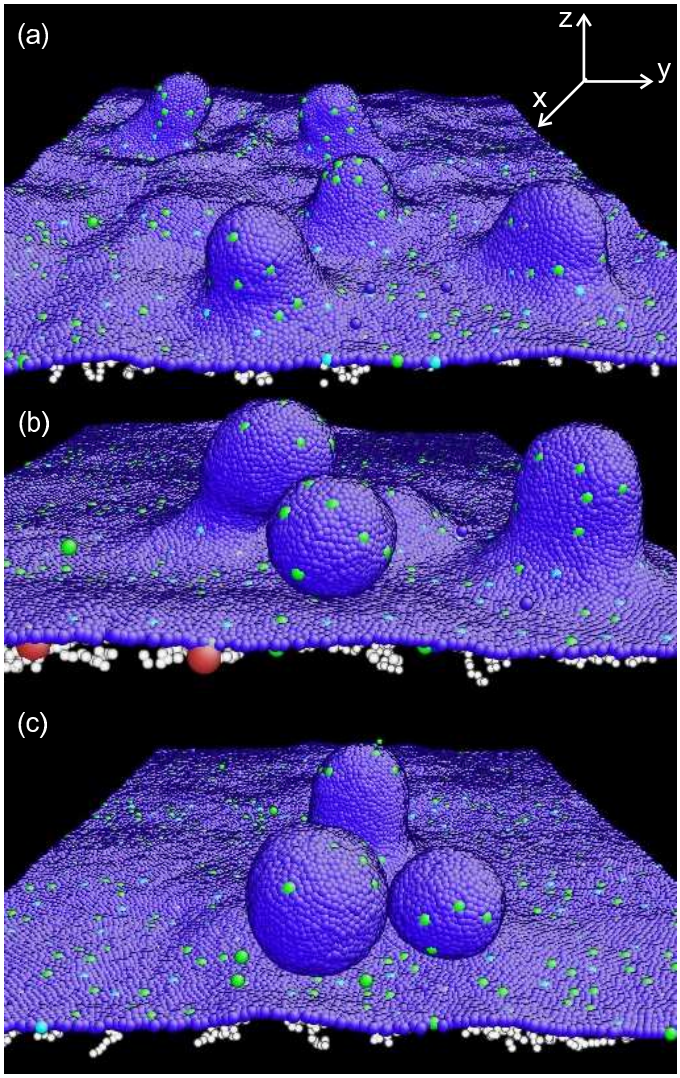

Figure 4 EC11454 23JUN2015

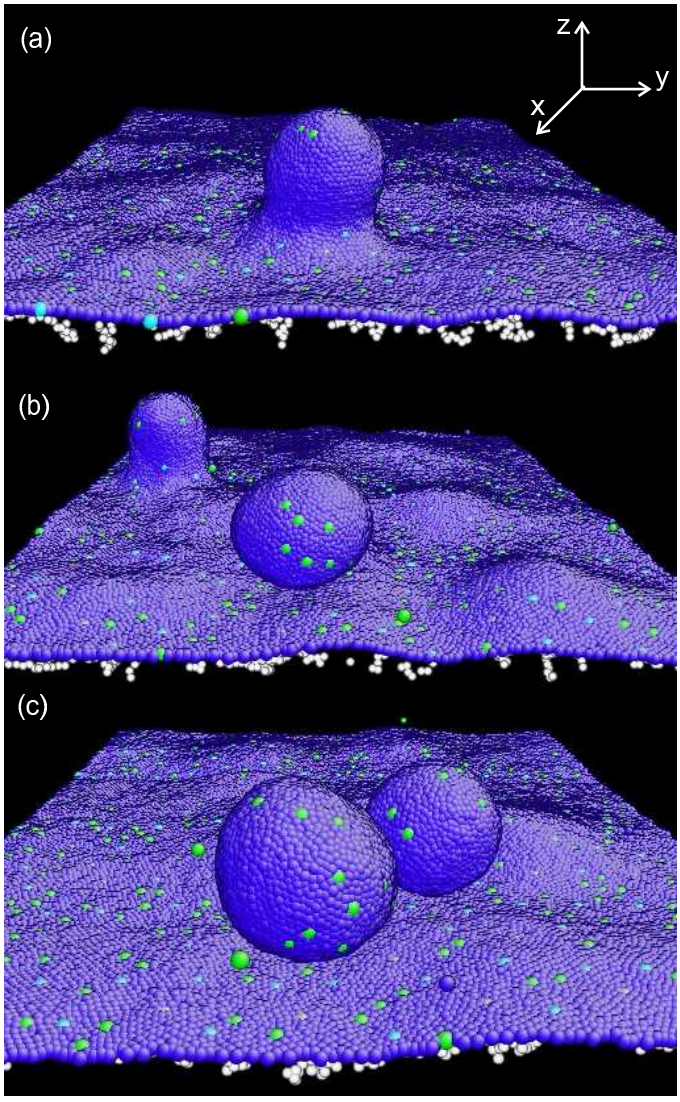

Figure 5 EC11454 23JUN2015

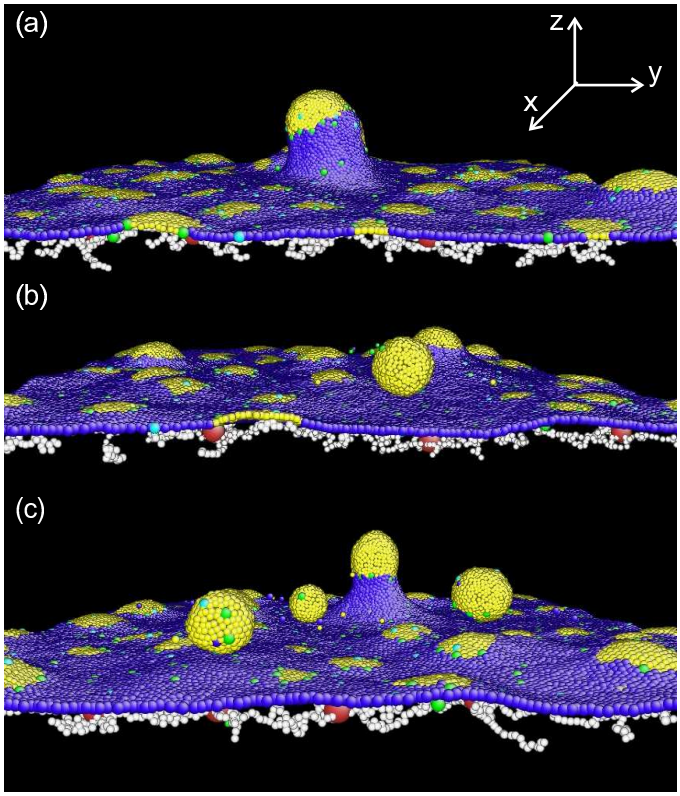

Figure 6 EC11454 23JUN2015

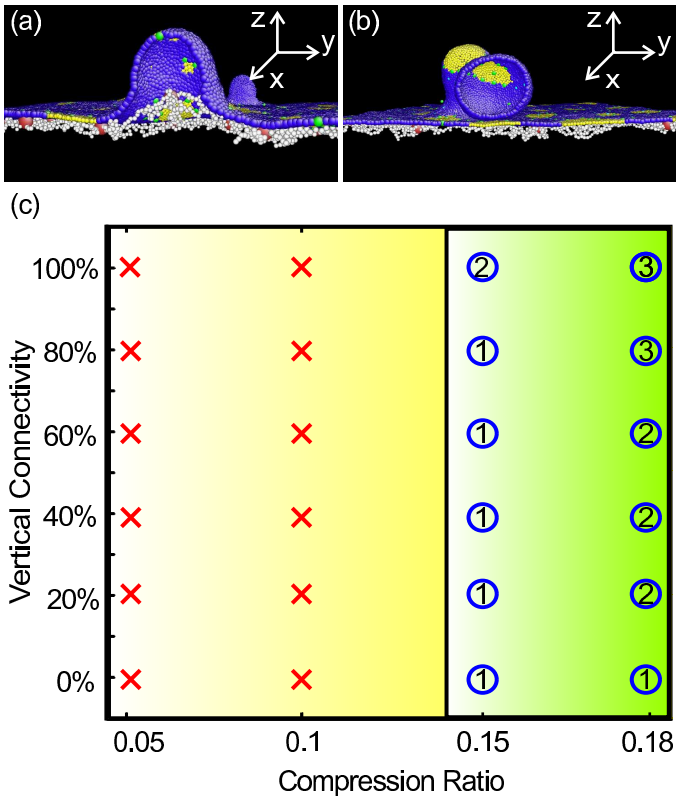

Figure 7 EC11454 23JUN2015

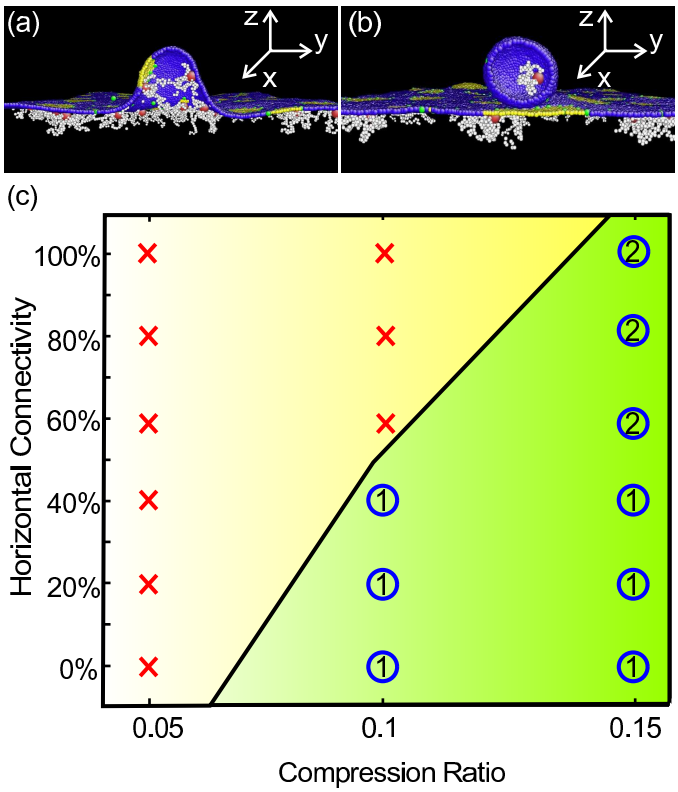

Figure 8 EC11454 23JUN2015